Combined soot optical characterization using 2-D multi-angle light scattering and spectrally resolved line-of-sight attenuation and its implication on soot color-ratio pyrometry

Bin Ma · Marshall B. Long

Abstract Soot characterization using multiple techniques has been performed in a series of nitrogen-diluted ethylene coflow laminar diffusion flames. Soot aggregate sizes have been measured in two dimensions, as opposed to traditional point measurements, by a newly developed two-dimensional multi-angle light scattering technique where image processing was applied to align images for Guinier analysis. Extinction measurements have also been performed using spectrally resolved line-of-sight attenuation with an imaging spectrometer. Spectrally and spatially resolved extinction measurements have been obtained as well. Combined with previously obtained time-resolved laser-induced incandescence measurements of primary particle diameters, the scattering and absorption components of extinction can be estimated. The so-called dispersion exponent that describes the wavelength dependence of spectral emissivity was determined in two dimensions and found to improve the accuracy of soot color-ratio pyrometry measurements.

1 Introduction

Soot is a type of fine particulate matter under 2.5 µm (PM2.5) produced from incomplete combustion of hydrocarbon fuels and is considered as an airborne contaminant with known adverse effects on human health. Strict regulations enacted on the emission of PM2.5 by air-quality agencies require tight control of soot formation, which in turn requires understanding of the formation mechanisms.

In the soot formation process, nearly spherical primary particles are first formed from large polycyclic aromatic hydrocarbon molecules and then agglomerate into larger mass fractal aggregates that may contain hundreds of primary particles [1]. Various in situ optical diagnostic techniques have been developed to characterize different properties of soot particles in point or planar measurements. For example, laser-induced incandescence (LII) is often used to determine soot volume fraction and primary particle diameter in two dimensions [2–6]. One-angle elastic light scattering (ELS) can be used to determine soot radius of gyration in two dimensions if combined with LII [7, 8]. Multi-angle light scattering (MALS), as an elastic light scattering technique, is often used to determine various aggregate parameters such as radius of gyration and fractal dimension, but is limited to point measurement [9–12]. In this work, two-dimensional multi-angle light scattering (2-D MALS) was developed and used in conjunction with spectrally resolved line-of-sight attenuation (spec-LOSA) to characterize N_2-diluted 60 and 80 % C_2H_4 (with 40 % N_2 and 20 % N_2 by volume, respectively) coflow laminar diffusion flames. The flames have been studied previously [13–18] and are target flames of the international sooting flame workshop [19]. The results are combined with previously acquired particle sizing measurements performed by time-resolved laser-induced incandescence (TiRe-LII) [14] to provide insight on soot spectral emissivity and to correct soot pyrometry temperature measurements.

Multi-angle light scattering (MALS) is a powerful tool to characterize soot aggregate properties. In particular, the soot aggregate size can be measured by a multi-angle scattering experiment performed in the so-called Guinier regime through a Guinier analysis. Gangopadhyay et al. [20] applied the approach in measurement of soot

B. Ma (✉) · M. B. Long
Department of Mechanical Engineering and Materials Science, Yale University, New Haven, CT 06511, USA
e-mail: bin.ma1@ge.com

aggregate size in a CH_4/O_2 premixed flame at several downstream points. The soot aggregate size was found to increase with height above the burner (HAB). Sorensen [10] provided an excellent review on the subject of light scattering by fractal aggregates, in which the multi-angle scattering technique was discussed in detail. Oltmann et al. [12] designed an experiment using an ellipsoidal mirror to collect the scattering signals from one point in a wide range of angles; this allows the determination of soot radius of gyration through single-shot acquisition of the full range of scattering angles. The approach was then applied in both laminar and turbulent flames, and good agreement was reported when comparing to TEM measurements [11]. All of the previous MALS measurements, however, have been restricted to point measurements according to the authors' knowledge. Two-dimensional full-field measurements are desired in order to better understand the soot formation process. In this work, the possibility of extending the Guinier analysis to two dimensions through proper image processing is demonstrated. Two-dimensional maps of the weighted average or effective radius of gyration [10, 11] are reported for N_2-diluted 60 and 80 % C_2H_4 coflow laminar diffusion flames.

Light extinction, sometimes referred to as line-of-sight attenuation (LOSA), has been extensively used for soot measurements [21–25]. The light beam from some source (e.g., a laser or lamp) is arranged to traverse the absorbing media (i.e., the flame) before reaching a detector. The light attenuation can be determined by taking ratios of the attenuated beam over the non-attenuated beam and can be used to determine the soot volume fraction, or even soot optical properties if combined with other measurements. The spec-LOSA technique is a further modification of LOSA made by Coderre et al. [26] that incorporates an imaging spectrometer to measure light attenuation as a function of wavelength. This technique has been applied to investigate the optical properties of both cooled soot [26] and in-flame aging soot [27] at several downstream locations. In the current work, spec-LOSA has been used to measure soot extinction over the full sooty region of N_2-diluted 60 and 80 % C_2H_4 coflow laminar diffusion flames by sequential measurements at different vertical heights above the burner. Spatially and spectrally resolved line-of-sight integrated extinction profiles are obtained, from which two-dimensional radially distributed extinction coefficient maps can be recovered by Abel inversion.

The measurements of flame extinction, soot radius of gyration and soot primary particle sizes are combined to determine the dispersion exponent that describes the wavelength dependence of soot spectral emissivity. The dispersion exponents are determined in two dimensions, which allows for the calculation of soot spectral emissivity for each pixel location. Previously acquired soot

temperatures determined by color-ratio pyrometry using a "nominal" constant value of the dispersion exponent [13] are compared to those determined using measured dispersion exponents. Uncertainty analysis on the pyrometry-derived temperature is also performed.

2 Two-dimensional multi-angle light scattering

2.1 Guinier analysis

Multi-angle light scattering has been performed in the so-called Guinier regime to determine the effective soot aggregate size through a Guinier analysis. Excellent theoretical reviews on light scattering by fractal aggregates are available in Refs. [9, 10], and only a brief introduction is presented here. An essential equation to describe soot aggregates is expressed as Eq. (1),

$$N = k_0 \left(\frac{R_g}{a}\right)^D \tag{1}$$

where N is the number of primary particles in an aggregate, k_0 is a proportionality factor of order unity, R_g is the radius of gyration and is defined as the root mean square of the distances between each primary particle and the center of mass of the aggregate, a is the radius of the primary particle, and D is the fractal dimension—normally in the range of 1.7–1.8 for soot [10]. The objective of aggregate sizing is to measure the parameter R_g, which is a representative parameter for aggregate size. In the scattering experiment, an important experimental parameter is the scattering wave vector $\vec{q}$ defined as the difference of the incident and the scattered wave vector, and its magnitude is shown in Eq. (2).

$$q = 4\pi\lambda^{-1}\sin(\theta/2) \tag{2}$$

The magnitude of the scattering wave vector $\vec{q}$ can be set by choosing the laser wavelength λ and detection angle θ. For monodisperse aggregates composed of monodisperse primary particles, the scattered light intensity can be expressed as follows under the approximations that primary particles are in the Rayleigh limit and each primary particle scatters independently:

$$I_{sca}(q) = I_{inc}nN^2V\frac{d\sigma^p}{d\Omega}S(qR_g) \tag{3}$$

where I_{inc} is the incident laser intensity, n is the aggregate number density, N is the number of primary particles in a soot aggregate, V is the measurement volume, $\frac{d\sigma^p}{d\Omega}$ is the scattering cross section of a primary particle, and $S(qR_g)$ is the so-called structure factor, which is dependent on the radius of gyration. It can be seen that the ratio of the

scattered signal $I_{sca}(0)$ at $\theta = 0$ and $I_{sca}(q)$ at a certain angle is a function of only the structure factor and simple geometric relationships that cause V to change with the angle. All other parameters are isotropic at any angle and cancel out. Furthermore, when the aggregate size is smaller or close to q^{-1} (the length scale of the scattering) in the so-called Guinier regime (i.e., $qR_g \leq 1$), the ratio can be approximately expressed by Eq. (4), which forms the basis of the Guinier analysis.

$$I_{sca}(0)/I_{sca}(q) = S(0)/S(qR_g) \approx 1 + \frac{1}{3}q^2R_{g,\text{eff}}^2,$$
$$qR_g \leq 1 \quad \frac{I_{sca}(0)}{I_{sac}(q)} < 2 \tag{4}$$

For real soot aggregates that are polydisperse, the measured radius of gyration must be considered as an effective value $R_{g,\text{eff}}$ that has the physical meaning of being a weighted average as defined by Eq. (5) with the polydispersity of the monomer radius, which should be significantly smaller than that of the aggregates, neglected [28]. The value of $R_{g,\text{eff}}$ is generally greater than the arithmetic mean since it is strongly influenced by the large end of the distribution, but it still provides insight into the size of aggregates.

$$R_{g,\text{eff}}^2 = \frac{\int N^2 R_g^2(N)n(N)\mathrm{d}N}{\int N^2 n(N)\mathrm{d}N} = a^2 k_0^{-\frac{2}{D}}\frac{M_{2+2/D}}{M_2} \tag{5}$$

where $n(N)$ and $R_g(N)$ are the distributions of number density and radius of gyration of the aggregate, respectively. The moment term M_i is defined by Eq. (6) as

$$M_i = \int_{N=1}^{N=\infty} n(N)N^i\mathrm{d}N \tag{6}$$

A routine procedure to determine $R_{g,\text{eff}}$ is to first obtain the scattering signal ratios through a multi-angle scattering experiment and then plot the ratios as a function of q^2. The effective radius of gyration $R_{g,\text{eff}}$ can then be obtained from a linear curve fitting with the slope equal to $\frac{1}{3}R_{g,\text{eff}}^2$. The range of $I_{sca}(0)/I_{sca}(q)$ with good linearity is normally extended up to a value of 2 [10, 12]. Therefore, the Guinier

evaluation range of this study is also bounded by $I_{sca}(0)/I_{sca}(q) < 2$.

2.2 Experimental setup

The experimental setup for two-dimensional multi-angle light scattering is shown in Fig. 1. The flames investigated in this work are sooting, axisymmetric, laminar diffusion flames operating under 1 atm at 298 K. The fuel consisted of 60 and 80 % C_2H_4 by volume, with the balance being N_2. The burner consists of a 0.4-cm-inner-diameter vertical tube, surrounded by a 7.4-cm-diameter coflow. The fuel velocity at the burner surface had a parabolic profile, and the air coflow was plug flow, both with average velocities of 35 cm/s. The burner was mounted on a programmable stepping motor for vertical movement. A frequency-doubled 532 nm Nd:YAG laser (Continuum PL-8010) with a repetition rate of 10 Hz provided the illumination. A 300 mm focal length cylindrical lens focused the laser to a vertical sheet that traversed the center of the flame. The laser sheet thickness is measured to vary from 72 μm at the flame centerline to 81 μm at a radius of 3 mm near the luminous edge of the flame. The long focal length lens is preferred to provide a nearly constant beam thickness across the flame. Nevertheless, slight variation of beam thickness is not critical since a divergent beam increases the sample volume while proportionately decreasing with laser fluence. The total signal is kept relatively constant. The laser sheet was spatially cropped by an aperture to ~ 7 mm in height. The flame was sequentially measured at different heights by vertically moving the burner in steps of 2 mm using a stepper motor. The central region of the laser sheet, where the intensity is more stable and evenly distributed, was used for signal evaluation and used to composite the full flame information. Similar results were obtained if the central 4 mm region was used to composite the full flame image, but only the results of the 2 mm case are shown in this paper. A neutral density filter was placed in the optical path to attenuate the laser beam to an energy level of ~ 5 mJ per pulse to prevent laser-induced

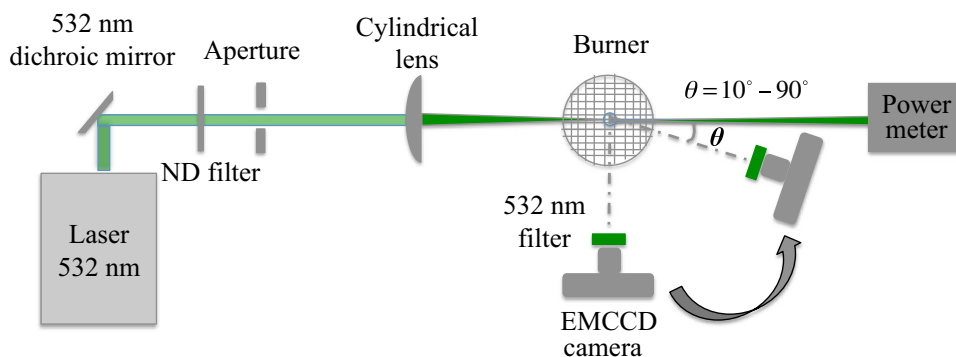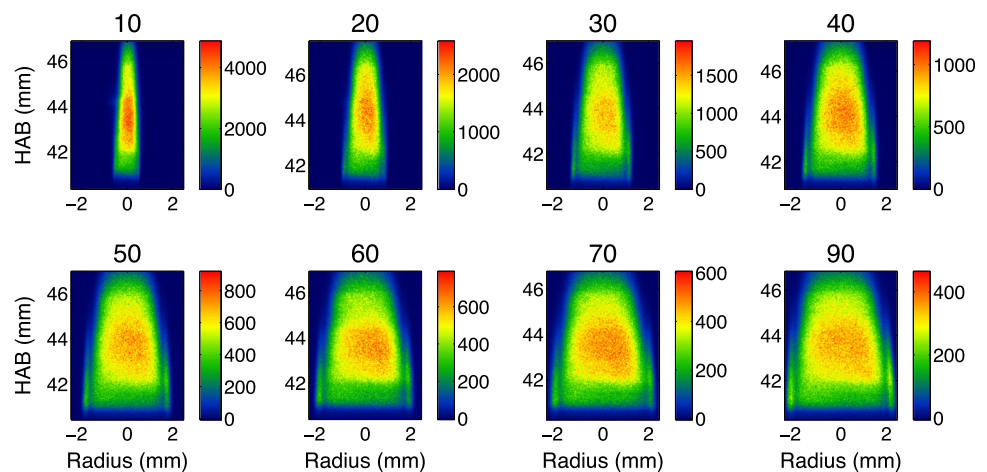Fig. 1 Two-dimensional multi-angle light scattering setup

Fig. 2 Background-subtracted and signal-averaged scattering images taken at 10°–90° detection angles as specified. The data are from a region near the tip of the 60 % flame with signal values expressed as average CCD counts

incandescence (LII). Negligible LII signal was verified by comparing the signals at 431 nm (collected through a narrowband interference filter) with the laser turned on and off. A pyroelectric power meter (LaserProbe RjP-734) was used to monitor the laser energy and to stop the beam. The measured laser energy was used for signal normalization to account for laser power fluctuations and drift.

The multi-angle scattering experiment involves imaging the soot-scattered signal at a set of angles. The detector was a cooled interline EMCCD camera (Andor Luca S) with 658 × 496 pixels and a pixel size of 10 μm. The camera was operated using the shortest available gate time of 470 μs. The camera was attached to a bar that rotated concentrically about the burner. The distance between the camera and the burner was fixed at 25 cm to ensure the same collection efficiency at each angle, and each image was centered on the burner. The detection angle between the lens optical axis and the laser beam was varied from 10° to 90°. Since the distance between the camera and the burner (25 cm) is much larger than the maximum flame diameter (~7 mm), the variation of detection angle as a function of position in the image can be neglected. A 50-mm focal length camera lens with extension tube was coupled to the detector. The horizontal spatial projection onto a single pixel varied from 25 μm at a detection angle of 90° to 144 μm at a 10° detection angle. A sufficient depth of field (i.e., greater than the maximum flame diameter of ~7 mm) was maintained with the f-number set at 16 such that even at the 10° detection angle, the entire flame scattering image remained in good focus. This was verified by comparison of target images at different angles, which is discussed in the next section. Each image was averaged over 50 laser shots to minimize the effect of small spatial variations of the flame caused by room air currents. For the sooty flames investigated in the study, the scattering signal is significantly greater (~2 orders of magnitude greater in the sooty region) than flame luminosity.

Nevertheless, flame background images were also acquired in the same way with the laser turned off and subtracted from the scattering signal images.

2.3 Image processing

The entire flame was sequentially imaged from upstream to downstream. However, only images at one downstream location are shown in this section to illustrate the image processing procedure. Raw scattering images taken at different angles from 10° to 90° are shown in Fig. 2. The image at the right-bottom corner is a normally observed image viewed at a 90° detection angle. When the camera was rotated around the burner to a smaller detection angle, the observed images became narrower in shape and the signal on each pixel was increased due to an increased sample volume as illustrated in Fig. 3. The sample volume illuminated by the laser beam and then projected onto a pixel is shown as a red-shaded area and varies with detection angle. At angle θ, the sample volume $V(\theta)$ is a factor of $1/\sin(\theta)$ greater than the sample volume at an angle of 90°. The soot distribution is assumed to be uniform over the small sample volume, and therefore, the signal is expected to increase by a factor of $1/\sin(\theta)$ from the 90° detection angle to a smaller detection angle θ.

To perform the Guinier analysis in two dimensions, the raw images must be first transformed to images with good spatial coincidence so that the ratio can be directly taken on a pixel-by-pixel basis. The spatially transformed images must then be re-sampled to carry the correct intensity information (i.e., pixel value). In this work, the image transformation was performed through bilinear image warping in Matlab [29]. Image warping involves a geometric mapping from the coordinate space of a source image to that of a destination image and a re-sampling procedure to determine the destination signals through an interpolation based on source signals. Bilinear image

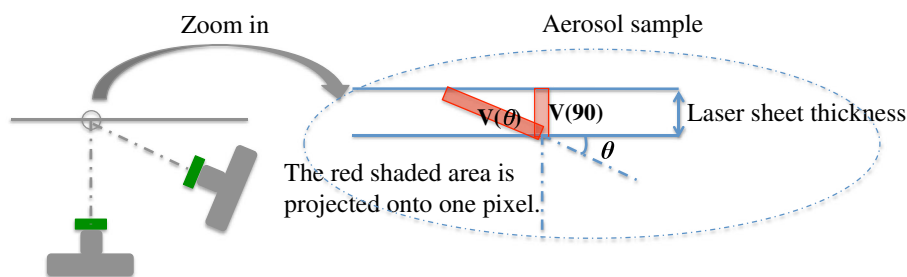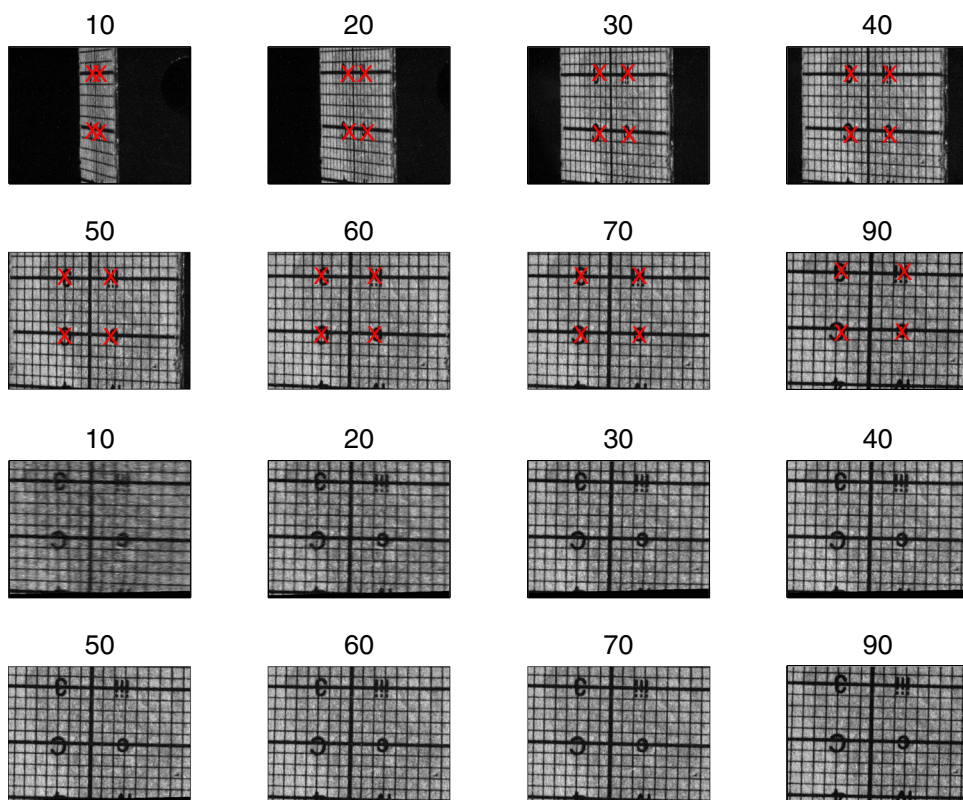**Fig. 3** An illustration of the increased sample volume at a decreased detection angle

Zoom in

Aerosol sample

$V(\theta)$ $V(90)$ Laser sheet thickness

θ

The red shaded area is projected onto one pixel.

Fig. 4 The original target images (*top*) and spatially transformed target images (*bottom*)

10 20 30 40

50 60 70 90

10 20 30 40

50 60 70 90

warping is an eight parameter warping that can be used to transform an arbitrary quadrilateral in the source image to an arbitrary quadrilateral in the destination image. The source coordinate (x,y) is correlated with the destination coordinate (u,v) through Eq. (7) [30].

$$u = a_{10}x + a_{01}y + a_{11}xy + a_{00}$$
$$v = b_{10}x + b_{01}y + b_{11}xy + b_{00} \tag{7}$$

where a_{ij} and b_{ij} are the eight parameters that can be solved given an initial source/destination image pair. To determine the eight parameters in Eq. (7), an engineering graph paper consisting of an equally spaced grid was used as a target. The target was fixed in the plane of the laser sheet, centered on the burner nozzle. Target shots were taken at a set of detection angles as shown in the top of Fig. 4. The 90° shot was chosen as the destination image while others are the source images. The same four non-collinear points

on the target shots were chosen in each image as illustrated by the red crosses. For every pair of source/destination images (e.g., 10°/90° or 70°/90°), four points (eight coordinate values) were used to solve for the eight parameters using Eq. (7). After the parameters were solved, the target shots in the source coordinates were spatially transformed into new images in destination coordinates as shown in the bottom of Fig. 4. Re-sampling of the images was performed by a bilinear interpolation. Good spatial coincidence was achieved in the transformed images. The images at smaller detection angle (e.g., at 10°) are seen to be blurrier mainly due to their smaller spatial resolution in the original image, which is a factor of $\sim$5.8 [sin(90°)/sin(10°)] smaller than the resolution at the 90° detection angle. An estimate of the spatial mismatch between the images can be obtained by considering the standard deviation in pixel locations between intersecting grid points in

Fig. 5 Warped scattering images at 10°–90° detection angles
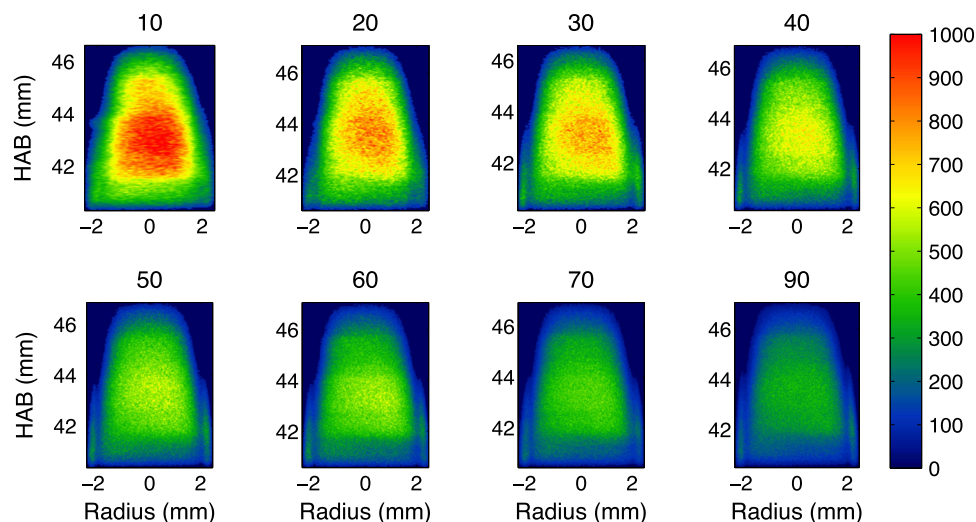
the transformed target images. By considering 4 random pixels over the central 2 mm region used for the composite flame images, maximum standard deviations of 0.091 and 0.096 mm were found in the radial and axial directions, respectively.

The same spatial transformation and signal interpolation procedure were then applied to the background-subtracted scattering images. The images were then normalized by a factor of $1/\sin(\theta)$ at each detection angle θ due to sample volume considerations shown in Fig. 3. The warped scattering images were cropped and are shown in Fig. 5.

As can be seen, two small peaks, possibly a result of different temperature-time history of soot particles, at a radius of 2 mm are visible in images taken at angles from 30° to 90°; however, they are not clearly visible in the images taken at 10° and 20°. This is expected since for imaging at small detection angles, fine features (e.g., large gradients) are not well resolved due to the smearing effect as shown in Fig. 6. For the normal view, the features at different depths of the sample volume will project onto the same location on the CCD. In contrast, at a small detection angle θ, the projection of features at different depths of the sample volume will be slightly shifted on the CCD, with the maximum shift ($72 \times \cos(\theta)$ μm) occurring at the front and back surface of the sample volume (based on the measured laser beam thickness of 72 μm). In the case of $\theta = 10°$, the shift spans roughly 7 pixels. Such a shift creates smeared images at small detection angles and fails to capture large gradient features as seen in both Figs. 4 and 5, where the images at 10° and 20° are blurred and do not preserve the steep gradients (i.e., the peaks) at a radius of 2 mm. When taking ratios of the image at 10° (without peaks) over images at other different angles (with peaks) for the Guinier analysis, the ratio images will contain artificial peaks due to the
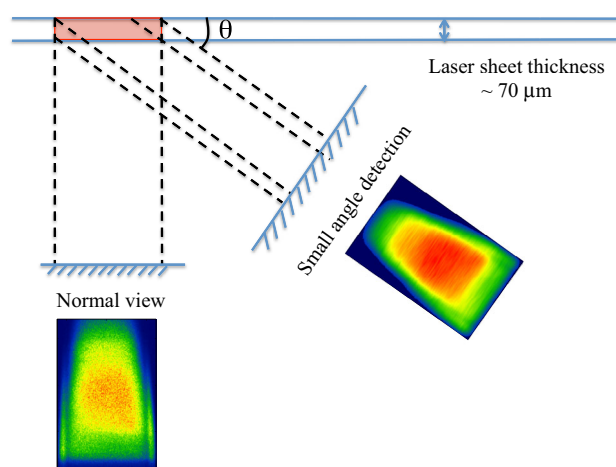

Fig. 6 An illustration of the smearing effect at a small detection angle. Here, the small angle detection image was calculated based on the normal view image

smearing effect. To address this problem, images taken at angles from 20° to 90° were all degraded via image processing to the 10° viewing angle, in order to match the spatial resolution and, more importantly, to match the smearing effect. The image degradations were performed based on computer simulations of the smearing effect. The sample volume was first sliced into at least ten layers along the depth of the sample volume, and each layer was projected onto the CCD plane with a slight spatial shift. The summation of the projected layers is the simulated smeared image shown in Fig. 6, where its normal view image was also shown for comparison.

The purpose of image processing in this work is to transform images taken at different angles into spatially coincident images, as a preparation for taking ratios on a pixel-by-pixel basis for the Guinier analysis in two

Fig. 7 Ratio images of $I(10)/I(\theta)$ without the smearing correction (*top*) and with the smearing correction (*bottom*)
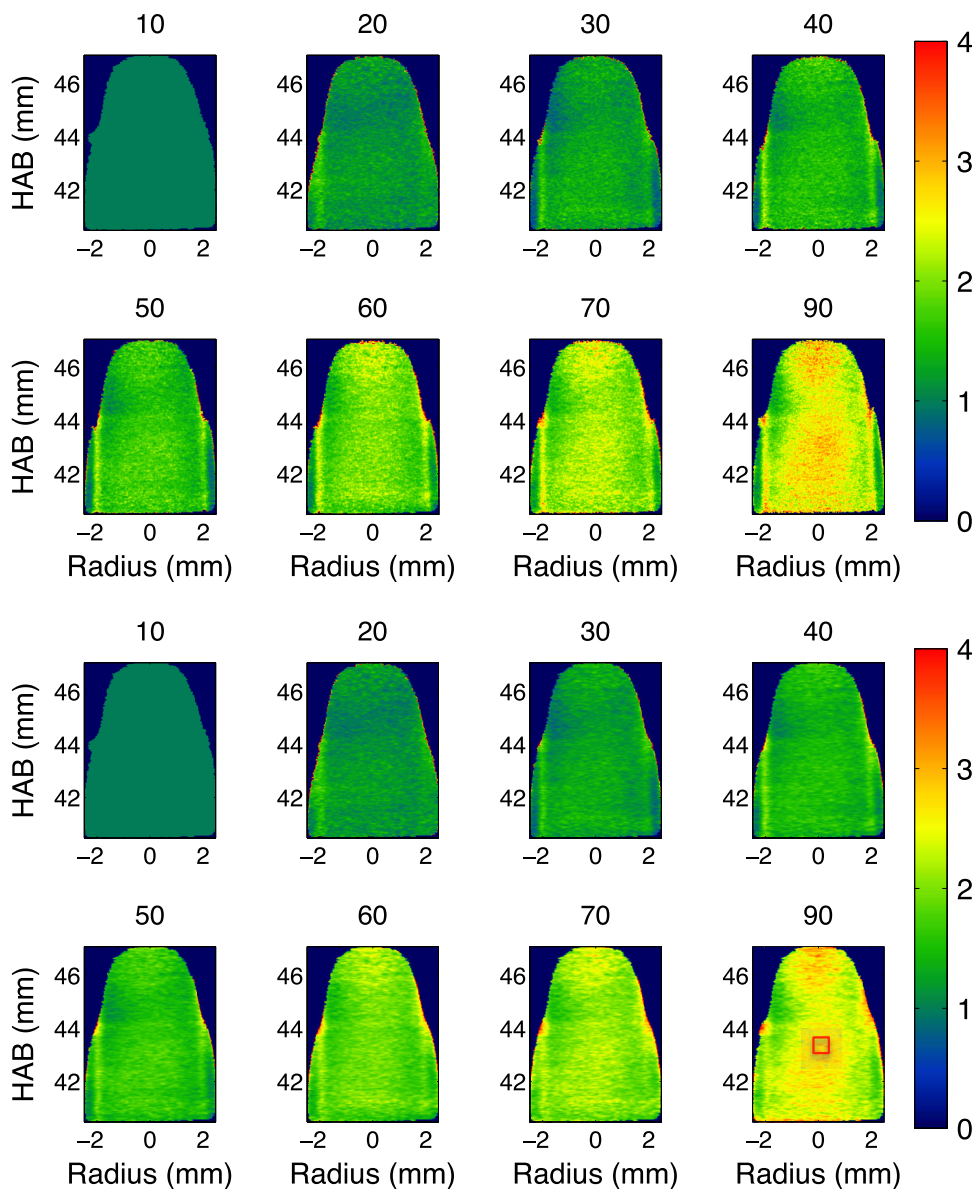
dimensions. During the image processing, it is important to make sure that the final warped images still carry the correct intensity signals. A useful check is to compare the total signal value of the original image and the warped image, as this total value should not be significantly altered by various image processing steps. The total signal was calculated by summing up all the pixel values in the frame, with any pixels outside the scattering region set to zero. The ratio of the total signal of raw images and warped images are calculated to be close to unity with variations less than 3 %.

Following the Guinier analysis, ratios of the $I(0)$ image over $I(\theta)$ image were taken. Since it is not possible to obtain the scattered signal at strictly 0°, 10° is often used as the smallest angle for taking ratios [10, 11]. The approximation tends to reduce the derived radius of gyration

somewhat, with the greatest effect for larger aggregates. However, even for the largest $R_{g,\mathrm{eff}}$ reported here, the error is ∼ 3 %. The ratio images without and with smear correction are shown in Fig. 7 in the top row and bottom row, respectively. The ones with smear correction are better at removing the artificial peaks on the wings.

Average values were calculated for a small region in each of the ratio images and are shown as a function of q^2 in Fig. 8. The position of the small region is illustrated by a red rectangle shown in the last image in Fig. 7. Good linearity is obtained in the Guinier evaluation range where $I_{\mathrm{sca}}(0)/I_{\mathrm{sca}}(\theta) < 2$. A linear curve fitting was performed in the range, and a R^2 value of 0.992 was obtained as a representation for the goodness of fitting. $R_{g,\mathrm{eff}}$ was determined to be 130.1 nm from the slope of the fitted curve.
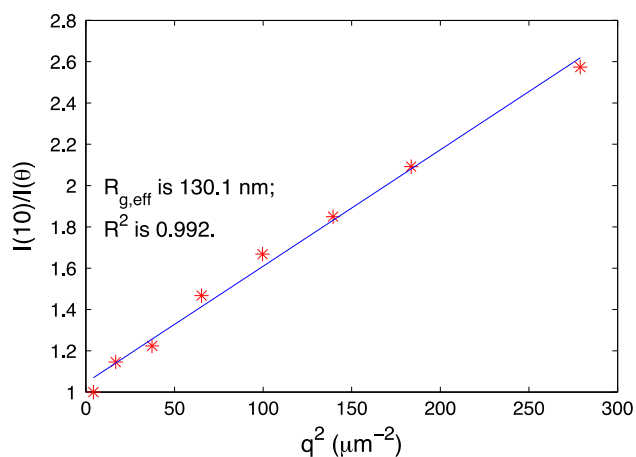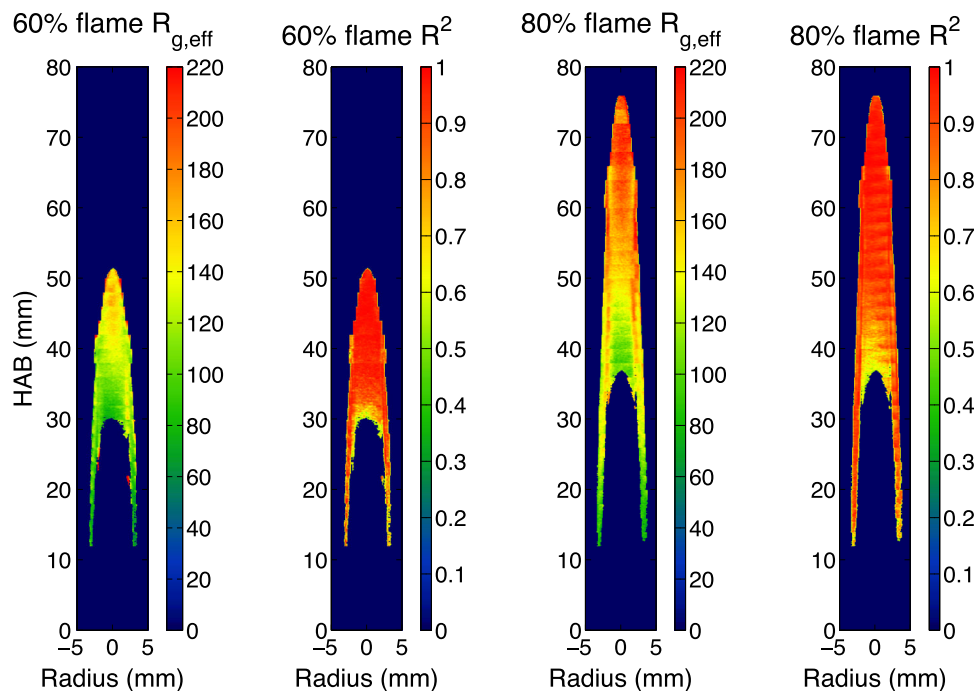
Fig. 8 The measured ratio of $I(10)/I(\theta)$ plotted as a function of q^2 (*red dots*) and a linearly fitted curve (*blue line*)

The flame was sequentially measured at different heights by vertically moving the burner in steps of 2 mm using a stepper motor, and the above procedure was performed for each pixel at each height. Full flame $R_{g,\text{eff}}$ and R^2 maps of the 60 % C_2H_4 and 80 % C_2H_4 coflow laminar diffusion flames are composited and shown in Fig. 9. A spatial filter based on R^2 maps was created to filter out $R_{g,\text{eff}}$ points with R^2 values less than 0.5. It should be noted that the data at the flame tip for the 80 % flame have a discontinuity at 73 mm HAB. This is mainly due to the fact that multiple images taken at different times, with small spatial fluctuations on the tip, were used to evaluate $R_{g,\text{eff}}$, and the fluctuating signals were likely to distort the slope of fitting and result in greater or smaller value of $R_{g,\text{eff}}$. The

$R_{g,\text{eff}}$ peaks along the wings may be problematic as well, since the intensity gradients of scattering images at these regions are large and a slight spatial mismatch could result in distorted ratios and therefore $R_{g,\text{eff}}$ values. The R^2 values are also observed to be relatively low at the upstream locations around HAB = 30 mm and HAB = 38 mm for 60 and 80 % flames, respectively. In these regions, the scattering intensities at the wings saturate much earlier than the intensities around the flame centerline. In order to obtain unsaturated images, the signals around the centerline were low and noisy, which results in lower R^2 values. These issues mentioned above might be improved in a future experiment by imaging the large gradient regions (e.g., the wings) with higher spatial resolution, and spatially filtering the wings to obtain greater signal around the centerline. Nevertheless, the R^2 values, generally greater than 0.9 except at the low signal regions, give confidence in the validity of the $R_{g,\text{eff}}$ values. The centerline $R_{g,\text{eff}}$ values for both flames are plotted in Fig. 10. Despite the noise of the plot, $R_{g,\text{eff}}$ is shown to monotonically increase with the HAB from 80 to 160 nm for the 60 % C_2H_4 flame and 100–200 nm for the 80 % C_2H_4 flame.

3 Spectrally resolved line-of-sight attenuation (spec-LOSA)

3.1 Experimental setup

The experimental configuration for making spectrally resolved absorption measurements along a radial line

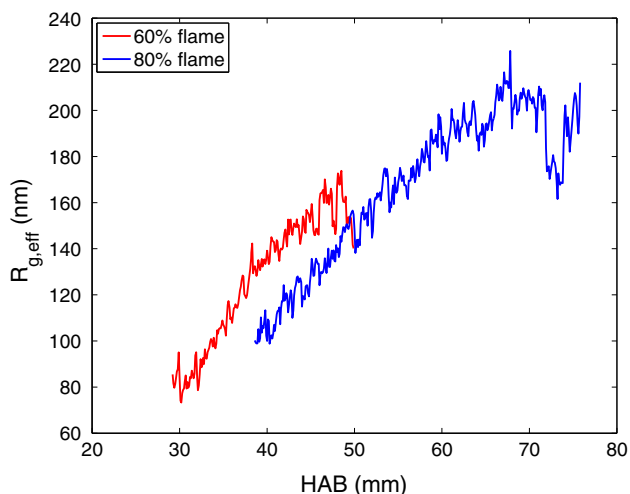**Fig. 9** Soot radius of gyration of the 60 and 80 % C_2H_4 flame and its corresponding R^2 maps

Fig. 10 Effective soot radius of gyration along the centerline of 60 and 80 % flames as a function of the height above the burner

through the flame is shown in Fig. 11. A high intensity illuminator (Dolan–Jenner Fiber–Lite series 180) was observed to provide stable output after a 20-min warm-up and was used as the light source. A 2-mm diameter aperture was placed in front of the light to provide a point source. Three spherical glass lenses, with focal length 200, 125 and 125 mm, respectively, were used to collimate and focus the light beam. The distance between the aperture and lens matches the focal length. The maximum angular dispersion due to chromatic effects between 400 and 750 nm is estimated to be $\sim 0.01°$. Therefore, parallel beams can be assumed to pass the flame and enter into the spectrograph as shown by the dashed lines. An externally controlled mechanical shutter was placed in the optical path and was synced with image acquisition to block or unblock the light source. A thermoelectrically cooled CCD camera (SBIG STF-8300M chip, 16 bits/pixel digitization, $3,326 \times 2,504$ pixels at 5.4 μm) was used in conjunction with an imaging spectrograph (Jobin Yvon CP200), with a 200-groove/mm grating and a 0.05-mm horizontal entrance

slit. The cooling temperature was stabilized at -10 °C to reduce thermal noise on the CCD chip.

Hyperspectral images were captured with the spatial coordinate along the radius of the flame and the spectral coordinate covering the range from 400 to 750 nm. The spatial projection is 5.95 μm per pixel, and the spectral dispersion is 0.14 nm per pixel. For this imaging configuration, the maximum flame width was smaller than the long dimension of the entrance slit. Therefore, the full width of the flame was imaged into the spectrograph without being clipped, which allowed the inversion of the natural log of the line-of-sight integrated transmissivity to obtain a radial profile of the extinction coefficients. The burner was mounted on a stepper motor to allow vertical movement. The flame was traversed at steps of 0.5 mm starting from 1 cm above the burner, below which there was no measurable visible light attenuation. For the 60 and 80 % flames, 90 and 130 steps were used to traverse the flames, respectively. Data acquisition was automated with the open source software OMA, which was used to control the movement of the stepper motor, image acquisition of the CCD camera and the open/close status of the mechanical shutter. At each height, with the flame kept ignited, transmission and emission images were acquired as the lamp was unblocked and blocked. A lamp image and dark background image were taken when the flame was turned off after scanning the whole flame to reduce the total experiment time. The final images are summations of five exposures of 0.2 s each, to average small spatial variations of the flame caused by room air currents as well as to improve the signal-to-noise ratio.

3.2 Image processing

A typical set of raw images is shown in Fig. 12. The TRANSMISSION image was taken when the flame and lamp were both turned on. The EMISSION image was taken when the flame was on but the lamp was blocked. The LAMP image was taken only once when the flame was
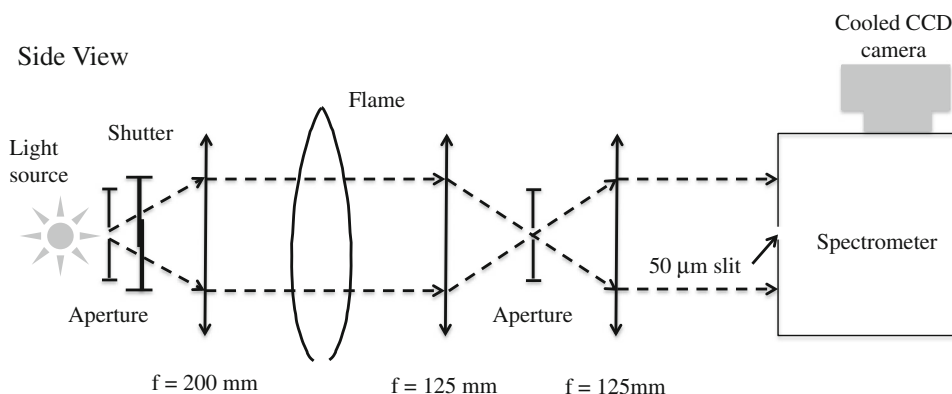
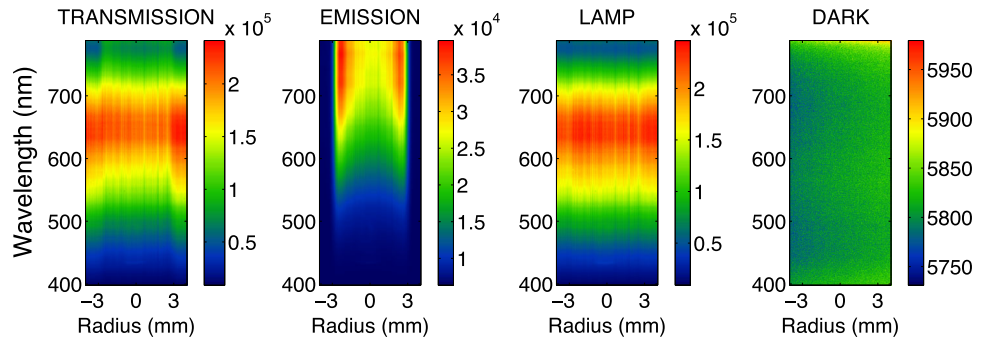**Fig. 11** Spec-LOSA experimental setup

Fig. 12 Sample raw images at a height of 35 mm above the burner for the 80 % C_2H_4 flame

turned off and lamp was unblocked. The DARK image was taken when the flame and lamp were both turned off.

The line-of-sight integrated spectral transmissivity, τ_λ, can be obtained via Eq. (8) and is shown in Fig. 13 on the left.

$$\text{Transmissivity } (\tau_\lambda) = \frac{\text{Transmission} - \text{Emission}}{\text{Lamp} - \text{Dark}} \quad (8)$$

Ideally, the transmissivity value outside the flame region should be one since there is no attenuating media. However, values from 0.99 to 1.01 were obtained since the LAMP image was taken at a time later than the TRANSMISSION image for the sake of overall experiment time, and the lamp intensity varied by ~ 2 % over the entire measurement time of ~ 80 min. In post-processing, appropriate factors were multiplied to the LAMP image at each height to compensate for the small variation of lamp intensity and to ensure unity in the integrated_τ map outside the flame region. The line-of-sight spectral transmissivity $\tau_\lambda(y)$ at a distance of y from the flame center can be calculated by Eq. (9) [31].

$$\tau_\lambda(y) = \exp\left[-\int_{-\sqrt{R^2-y^2}}^{\sqrt{R^2-y^2}} K_{\text{ext},\lambda}(x,y)dx\right] \quad (9)$$

where R and x are the flame radius and distance along the optical path, respectively. $K_{\text{ext},\lambda}$ is the spectral extinction coefficient. Since the flame is axisymmetric, the spectral extinction coefficients $K_{\text{ext},\lambda}$ can be determined by Eq. (10).

$$K_{\text{ext},\lambda} = Abelinv(-\ln(\tau_\lambda))/L \quad (10)$$

where $Abelinv(x)$ indicates that an Abel inversion operated on an axisymmetric image x, L is the effective extinction length that equals the depth of the projection onto a single pixel, and $\ln(\tau_\lambda)$ is the natural log of the spectral transmissivity image τ_λ. A three-point inversion algorithm [32, 33] was built into the OMA software to perform the Abel inversion. Since Abel inversion is very sensitive to noise, all images were 2×2 binned to reduce noise and image
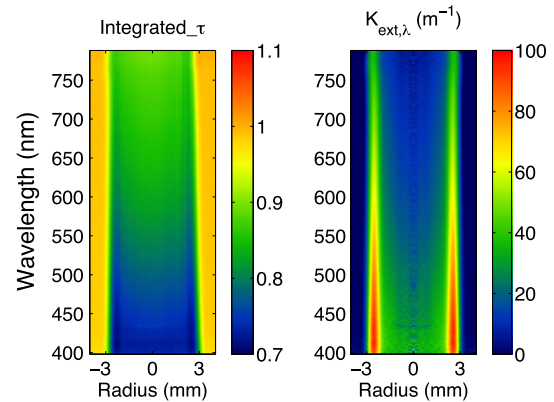

Fig. 13 Integrated transmissivity τ (*left*) and extinction coefficient $K_{\text{ext},\lambda}$ maps (*right*) at a height of 35 mm above the burner for the 80 % C_2H_4 flame

processing time. The spatial projection L is 11.9 μm after the image binning. Gaussian smoothing using a one-dimensional kernel with $\sigma = 5.71$ over 21 pixels was also applied along the radial direction before inversion to reduce the noise of the inverted images. Gaussian smoothing was chosen to effectively reduce noise while keeping the shape of the distribution. The smoothing parameters were chosen so that the processing time is relatively short and further smoothing did not improve the image signal/noise ratio significantly. The derived $K_{\text{ext},\lambda}$ map with units of m^{-1} is shown in Fig. 13 on the right.

The above images show varying spectral information at a fixed spatial height. A full flame scan was performed by traversing the flame vertically over the visible flame height. A two-dimensional spatial distribution can be composited with scans at different heights for the specific wavelengths. For illustration, images of line-of-sight transmissivity τ and extinction coefficient $K_{\text{ext},\lambda}$ maps of the 80 % flame at several discrete wavelengths (450, 550, 600 and 700 nm) are shown in Fig. 14 with corresponding radial line plots at 30 mm and 50 mm HAB. As can be seen, the transmissivity outside the flame region is very close to one as expected. Extinction gradually decreases with increasing
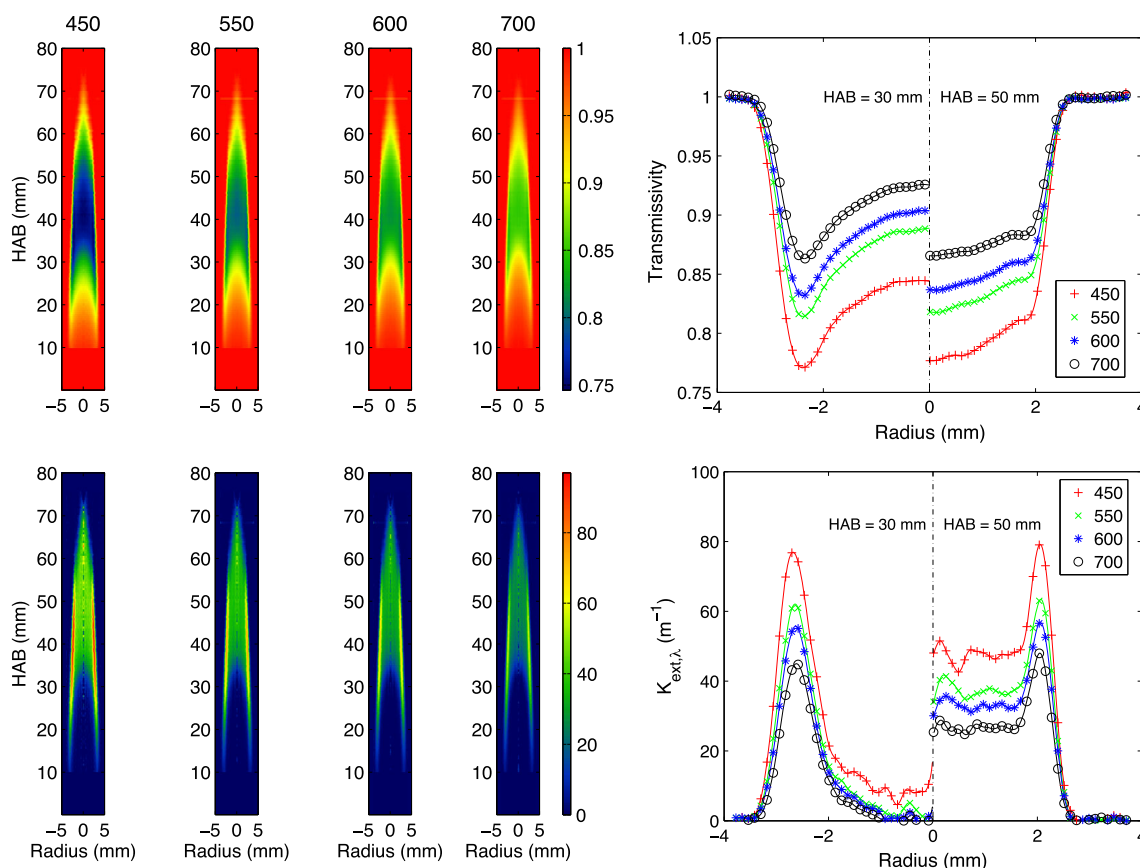
Fig. 14 Line-of-sight integrated transmissivity (*top*) and extinction coefficient $K_{ext,\lambda}$ (m^{-1}) maps (*bottom*) at 450, 550, 600 and 700 nm (from *left* to *right*) for the 80 % flame. Corresponding radial line profiles are also shown at HAB = 30 mm (*left*) and 50 mm (*right*)

wavelength, and greater extinction occurs on the wings of the flame as suggested by the $K_{ext,\lambda}$ maps. The peaks of the $K_{ext,\lambda}$ maps at different wavelengths also line up very well, which indicates that there is no obvious chromatic aberration associated with the optical setup.

4 Two-dimensional determination of the dispersion exponent

The dispersion exponent, α, is fundamentally dependent on the soot refractive index m and is introduced to describe the wavelength dependence of the soot absorption coefficient as shown by Eq. (11) [34–36].

$$K_{abs,\lambda} = \frac{36\pi E(m)f_v}{\lambda} \propto \frac{1}{\lambda^\alpha} \tag{11}$$

where $K_{abs,\lambda}$ is the soot absorption coefficient, $E(m)$ is the absorption function of soot which depends on the refractive index m, f_v is the soot volume fraction, and λ is wavelength. α is a non-unity value since $E(m)$ also has a wavelength dependence to be determined. Assuming the validity of

Kirchhoff's law, i.e., at thermal equilibrium, the emitted radiation is balanced with absorbed energy. The dispersion exponent can be related to the soot spectral emissivity via Eq. (12) [23, 36, 37], where L is the extinction length. Given $K_{abs,\lambda}L$ is a small value, the first order of the Taylor expansion can be used with good accuracy.

$$\varepsilon_\lambda = 1 - \exp(-K_{abs,\lambda}L) \propto K_{abs,\lambda} \propto \frac{1}{\lambda^\alpha} \tag{12}$$

The value of α is very important to color-ratio pyrometry and has been measured as a function of H/C ratio of soot and reported to vary with flame downstream locations. It has been reported to be ~ 2.2 for young soot with H/C ratio of 0.5–0.6, and the value decreased to ~ 1.2 for more mature soot with H/C ratio of ~ 0.2 [35, 38, 39]. The value of 1.2 falls into the range of 0.65–1.43 that was measured by many studies with different fuels and summarized in [23] for the visible light range. In our previous work [13], a constant value of 1.38 was used for temperature measurement in the same flame as investigated here. However, this value is obtained from different flames and neglects spatial variations in flames [23, 37]. To the best of the authors'

knowledge, all ratio pyrometry studies to date have used some "nominal" constant value for α. It is the objective of this study to obtain a spatially resolved two-dimensional α map and to determine more accurate temperatures using the two-dimensional α map rather than a single value.

The value of α is determined from exponential fitting of the absorption coefficient $K_{\text{abs},\lambda}$ as shown in Eq. (11). $K_{\text{abs},\lambda}$ is obtained from the spec-LOSA measurement of $K_{\text{ext},\lambda}$ coupled with a correction for the scattering/absorption ratio $\rho_{\text{sa},\lambda}$ as shown by Eq. (13).

$$K_{\text{abs},\lambda} = \frac{K_{\text{ext},\lambda}}{1 + \rho_{\text{sa},\lambda}} \tag{13}$$

The scattering/absorption ratio $\rho_{\text{sa},\lambda}$ was determined from the primary particle sizes determined with TiRe-LII and the $R_{g,\text{eff}}$ determined from the 2-D MALS measurements. The differential scattering cross section of an ensemble of polydisperse aggregates was calculated by Eq. (14) considering the aggregate size distribution. The total scattering cross section was calculated by integrating the differential cross section over the 4π angle as Eq. (15) [10].

$$\frac{d\sigma_{\text{sca}}^{\text{agg}}}{d\Omega} = \int\limits_{N=1}^{N=\infty} n(N) \frac{d\sigma_{\text{sca}}^{\text{pp}}}{d\Omega} N^2 S(q R_g(N)) dN \tag{14}$$

$$= \frac{d\sigma_{\text{sca}}^{\text{pp}}}{d\Omega} M_2 \left(1 - \frac{1}{3} q^2 R_{g,\text{eff}}^2\right)$$

$$\sigma_{\text{sca}}^{\text{agg}} = \int\limits_{0}^{2\pi} \int\limits_{-1}^{1} \frac{d\sigma_{\text{sca}}^{\text{agg}}}{d\Omega} \sin^2(\phi) d\cos(\phi) d\theta \tag{15}$$

$$= \frac{8}{3} M_2 \pi k^4 a^6 F(m) \left(1 + \frac{4}{3D} k^2 R_{g,\text{eff}}^2\right)^{-\frac{D}{2}}$$

where the structure factor $S(q R_g)$ takes the Guinier form by assuming the majority of the aggregates fall into the Guinier regime, $\frac{d\sigma_{\text{sca}}^{\text{pp}}}{d\Omega} = k^4 a^6 F(m)$ is the Rayleigh differential scattering cross section of a primary particle, k is the wave vector, M_i is the ith moment as defined previously, a is the primary particle radius, $R_{g,\text{eff}}$ is the effective soot aggregate radius of gyration, D is the soot fractal dimension (a commonly used value of 1.8 is assumed), and $F(m)$ is the scattering function of refractive index m. The total absorption of an ensemble of polydisperse aggregates was calculated by Eq. (16).

$$\sigma_{\text{abs}}^{\text{agg}} = \int\limits_{N=1}^{N=\infty} 4\pi N k a^3 E(m) n(N) dN = 4 M_1 \pi k a^3 E(m) \tag{16}$$

where $E(m)$ is the absorption function of refractive index m. Other parameters are as defined previously. The scattering/absorption ratio $\rho_{\text{sa},\lambda}$ can then be calculated as Eq. (17).

$$\rho_{\text{sa},\lambda} = \frac{\sigma_{\text{sca}}^{\text{agg}}}{\sigma_{\text{abs}}^{\text{agg}}} = \frac{\frac{8}{3} M_2 \pi k^4 a^6 F(m) \left(1 + \frac{4}{3D} k^2 R_{g,\text{eff}}^2\right)^{-\frac{D}{2}}}{4 M_1 \pi k a^3 E(m)}$$

$$= \frac{M_2/M_1}{(M_{2+2/D}/M_2)^{\frac{D}{2}}} \frac{\frac{8}{3} N_{\text{eff}}^2 \pi k^4 a^6 F(m) \left(1 + \frac{4}{3D} k^2 R_{g,\text{eff}}^2\right)^{-\frac{D}{2}}}{4 N_{\text{eff}} \pi k a^3 E(m)} \tag{17}$$

The effective number of primary particles N_{eff} that compose an aggregate is defined by Eq. (18) and is shown to equal the ratio of the two moments, which also validates the third equal sign of Eq. (17).

$$N_{\text{eff}} = k_0 \left(\frac{R_{g,\text{eff}}}{a}\right)^D = \left(\frac{M_{2+2/D}}{M_2}\right)^{\frac{D}{2}} \tag{18}$$

The value of N_{eff} is readily available using the measured effective radius of gyration $R_{g,\text{eff}}$ and primary particle radius a. There is a large discrepancy of the constant k_0 in the literature [40–42]. Its value is assumed to be the more often used 2.41 (equivalent to $k_f = 8.5$) as measured in Ref. [42]. The ratio of $F(m)/E(m)$ is curve fitted to a second-order polynomial in the visible range based on the tabulation available in Ref. [43]. As discussed in Ref. [26], this table of data is considered more appropriate for this work as opposed to other data measured from compressed soot pellets [44] or with soot morphology neglected [45]. The ratio $F(m)/E(m)$ serves as a scaling factor in the $\rho_{\text{sa},\lambda}$ calculation and contributes only small uncertainty in the scattering correction given the small magnitude of $\rho_{\text{sa},\lambda}$ [26]. In Eq. (17), the correction factor $(M_2/M_1)(M_{2+2/D}/M_2)^{-D/2}$, in conjunction with the use of effective radius of gyration, accounts for the aggregate polydisperse distribution. This factor can be determined once the aggregate distribution is known. In this work, we assume lognormal distribution with the geometric standard deviation $\sigma_g = 2$ and the median of the distribution $N_{\text{med}} = 30$ for the entire soot region. The correction factor is then evaluated to be 0.48 and is used in the calculation of $\rho_{\text{sa},\lambda}$. This is certainly a simplification since the correction factor should vary with spatial location as the distribution changes. A rigorous approach is to use SEM sampling as discussed in [26] to determine the distribution and moments. However, performing extensive sampling over many points in a non-premixed flame to yield 2-D distributions of N_{med} and σ_g remains an interesting challenge. Nevertheless, as will be shown in next section, the scattering correction has a rather small effect on the derived pyrometry temperature.

The dispersion exponent is obtained by exponentially fitting $K_{\text{ext},\lambda}$ and $1 + \rho_{\text{sa},\lambda}$ separately, and then subtracting one from the other as expressed by Eq. (19)

$$\alpha = \alpha_{\text{ext}} - \alpha_{sa} \tag{19}$$

Fig. 15 An illustration of the exponential fitting of $K_{\text{ext},\lambda}$ (*left*) and $1 + \rho_{\text{sa},\lambda}$ with $R_{g,\text{eff}} = 100$ nm and $a = 40$ nm (*right*)
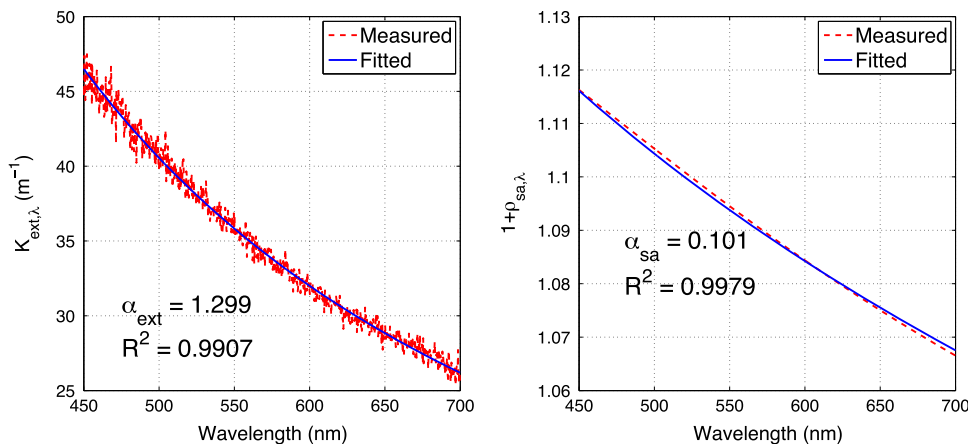
where α_{ext} and α_{sa} are the fitted exponents for $K_{\text{ext},\lambda}$ and $1 + \rho_{\text{sa},\lambda}$ as expressed by Eqs. (20) and (21), respectively.

$$K_{\text{ext},\lambda} \propto \frac{1}{\lambda^{\alpha_{\text{ext}}}} \tag{20}$$

$$1 + \rho_{sa,\lambda} \propto \frac{1}{\lambda^{\alpha_{sa}}} \tag{21}$$

The value of α obtained in this way is checked to be very close to that obtained by correcting the scattering component first via Eq. (13) and then performing the exponential fitting. Calculating α_{ext} and α_{sa} separately has the advantage of showing both values and helps to estimate the uncertainties. The exponential fitting of $K_{\text{ext},\lambda}$ at one flame location (1.5 mm radius at 35 mm HAB in the 80 % C_2H_4 flame) is plotted in Fig. 15 (left) as an example. Since the lamp signal used in the spec-LOSA experiment is relatively low at wavelengths below 450 nm, only wavelengths greater than 450 nm are used for the exponential fitting. The determined α_{ext} at this location is 1.299 with R^2 value of 0.9907. An exponential fitting of $1 + \rho_{\text{sa},\lambda}$ is also plotted in Fig. 15 (right) as an example. The $R_{g,\text{eff}}$ and a used in the calculation are 100 and 40 nm, respectively. The calculated $\rho_{\text{sa},\lambda}$ is in the range of 0.07–0.12, and the determined α_{sa} is 0.101.

The same fitting procedure was then performed for the entire soot region of the flame to obtain the 2-D spatially resolved α. Multiple measurements on the same flame are required for such determination, and their results are summarized in Fig. 16. The primary particle diameter (D_p) has been measured in previous work by time-resolved laser-induced incandescence (TiRe-LII) [14]. The effective radius of gyration ($R_{g,\text{eff}}$) was measured by 2-D MALS as described in Sect. 2. The 2-D extinction coefficients were measured by spec-LOSA as described in Sect. 3, and the profile at 500 nm is shown as an example. The flame emission is captured by a color digital single lens reflex (DSLR) camera (Nikon D300s). The radially resolved differential flame emission shown here is obtained by Abel-inverting the line-of-sight integrated emission image, which represents the emission signal from the flame sheet with thickness of the spatial projection of a binned pixel (11.9 μm). As can be seen, all measurements yield very good spatial overlap. A combination of these measurements was used to evaluate the spatially resolved dispersion exponent α at the spatial region where all measurements overlap.

The exponential fittings of $K_{\text{ext},\lambda}$ and $1 + \rho_{\text{sa},\lambda}$ for the full flame region return R^2 values generally greater than 0.98. R^2 values of α_{ext} decrease to 0.9 along the flame centerline due to the noisy Abel-inverted signals at this location. The spatially resolved two-dimensional dispersion exponent maps for α, α_{ext} and α_{sa}, along with their R^2 maps are shown in Fig. 17. The measured dispersion exponent is shown to vary with spatial location inside the flame corresponding to different degrees of soot aging. The determined α_{ext} value ranges from ~ 1 to ~ 2 across the entire sooty region and is much larger than the α_{sa} values from 0.03 to 0.16. The centerline α_{sa} values peak at 0.07 around HAB = 48 mm and decrease to 0.06 toward both upstream and downstream at HAB = 41 mm and 61 mm, respectively. In Ref. [27], $\rho_{\text{sa},\lambda}$ values were determined rigorously by considering the size distribution and reported for three heights (42, 50 and 55 mm) above the burner along the centerline of a similar ethylene/air coflow laminar diffusion flame (i.e., the Gülder flame). Adding one to the reference $\rho_{\text{sa},\lambda}$ values and then doing an exponential fit yielded α_{sa} values of 0.083, 0.088 and 0.070 for the three heights, respectively. Our measured values are not directly comparable to the literature values given the fact that the Gülder burner is different from our burner, and the Gülder flame operates at different flow rates without N_2 dilution. However, it is still interesting to see that the α_{sa} values obtained in our work and from Ref. [27] are comparable and differ by less than ~ 0.02. The value of α, after subtracting α_{sa} from α_{ext}, is found to be ~ 2 at upstream locations where the young soot is formed and is as small as ~ 0.9 on the wings of the flame where the soot is more mature.

Fig. 16 Soot measurements of primary particle diameter D_p, effective radius of gyration $R_{g,\text{eff}}$, spectral extinction coefficients $K_{\text{ext},\lambda}$ (only 500 nm is shown for illustration) and radially resolved differential emission signal on the 80 % C_2H_4 flame using TiRe-LII, 2-D MALS, spec-LOSA and Abel inversion of direct incandescence image, respectively
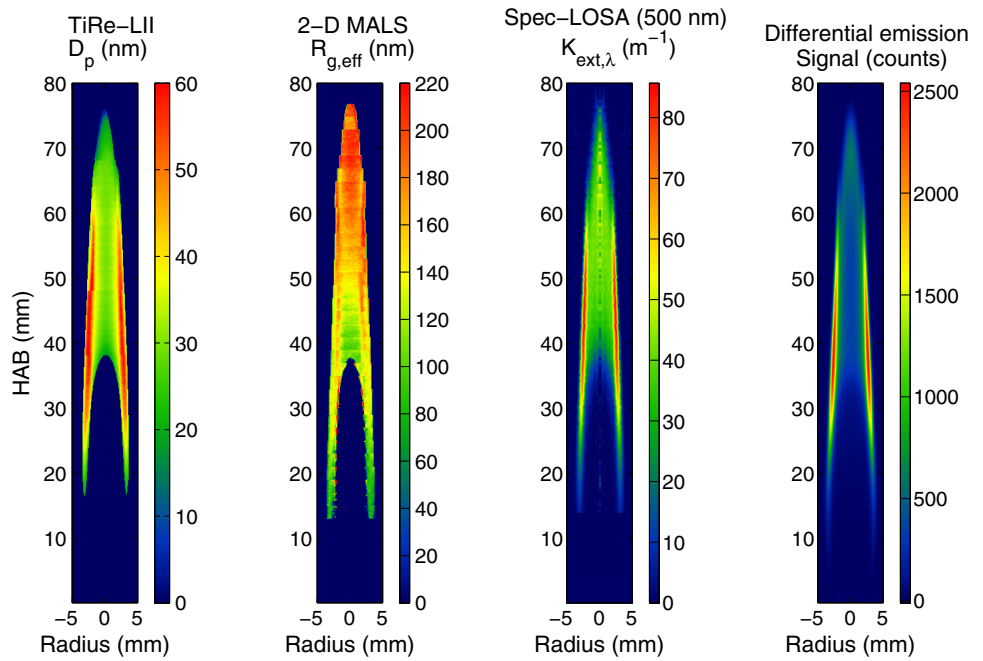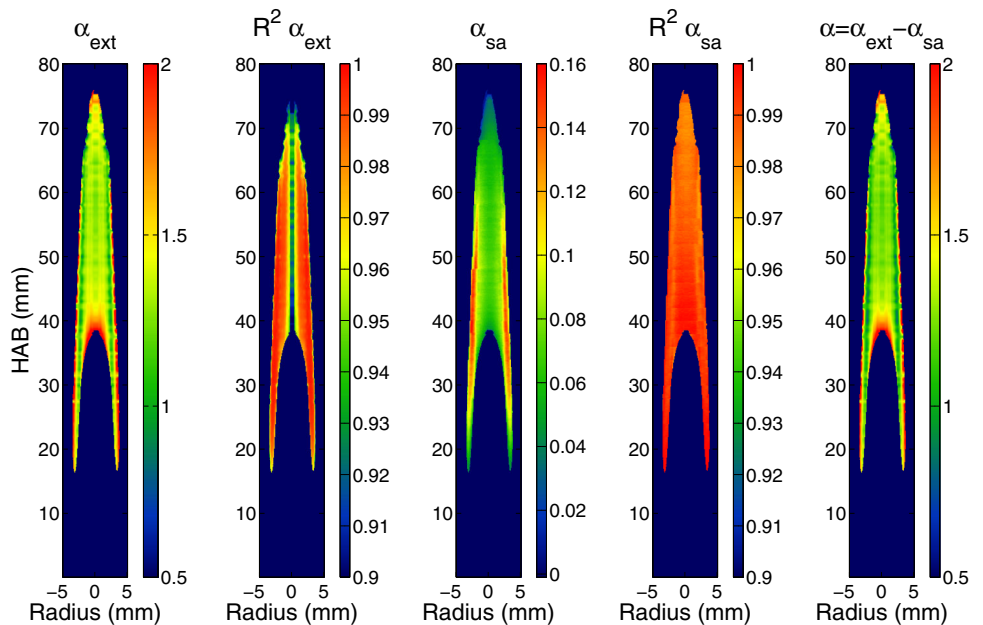
Fig. 17 Two-dimensional maps of α_{ext}, α_{sa} and their corresponding R^2 maps, and the dispersion exponent α for the 80 % C_2H_4 flame

5 Soot color-ratio pyrometry and temperature uncertainty

In our previous work as discussed in Ref. [13], soot emissivity was assumed to vary with $\lambda^{-1.38}$. Using the results from the previous section, the soot spectral emissivity can be calculated via Eq. (12) using measured α on a pixel-by-pixel basis. Lookup tables that correlate color-ratio and temperature are also calculated for each pixel location using Eq. (22),

$$\frac{S_{F_1}}{S_{F_2}} = \frac{\int \lambda^{-5} \eta_{F_1}(\lambda)\varepsilon(\lambda)[\exp(hc/\lambda kT)-1]^{-1}\mathrm{d}\lambda}{\int \lambda^{-5} \eta_{F_2}(\lambda)\varepsilon(\lambda)[\exp(hc/\lambda kT)-1]^{-1}\mathrm{d}\lambda} \quad (22)$$

where η_F is the detector spectral response of the DSLR camera with a BG glass filter in the setup and is shown in [46]. The camera characterization followed the same procedure as discussed in [13]. The measured α and a constant value of 1.38 along with their corresponding pyrometry temperatures and temperature differences are shown in Fig. 18.

Fig. 18 Measured and constant dispersion exponent and their corresponding ratio pyrometry temperatures and temperature differences
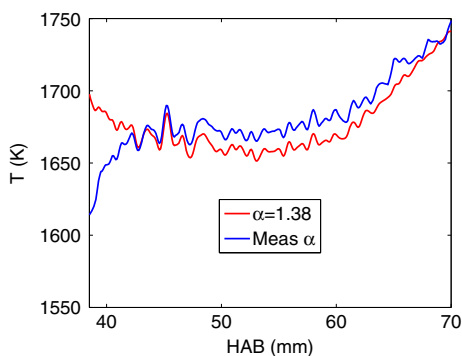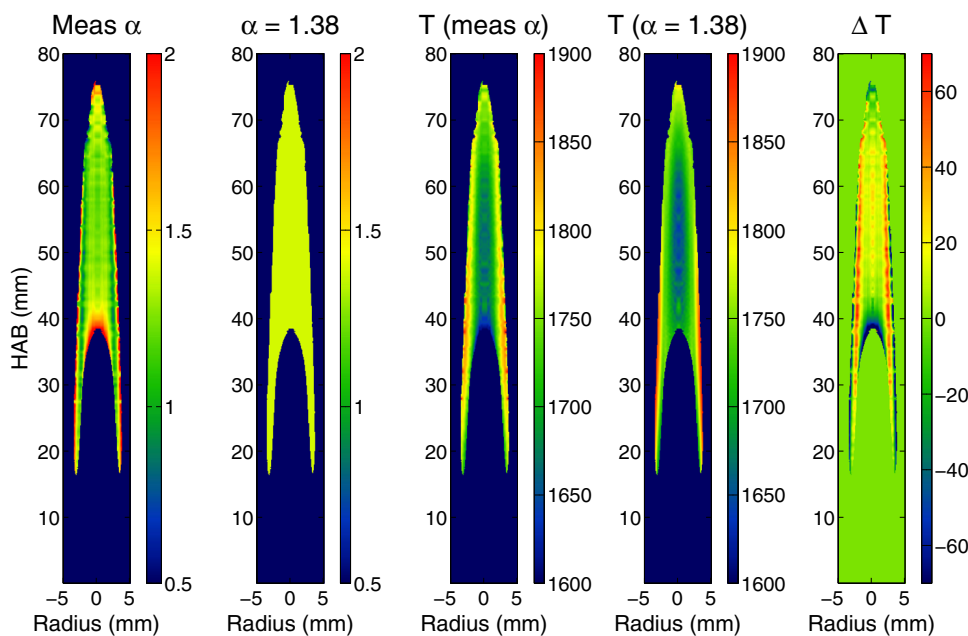

Fig. 19 Centerline pyrometry temperatures using measured the dispersion exponent α and *a* constant value of 1.38

The new temperature based on measured α has higher wing temperatures and lower upstream centerline temperatures than the old temperature based on a constant value of 1.38. The centerline temperature of both measurements is plotted in Fig. 19. The new temperature is more physically reasonable than the old measurements since the centerline temperature is expected to monotonically increase with HAB in the soot-containing region. The higher temperatures at heights below ~ 40 mm in the old measurements resulted from neglecting the spatial variation of α and the value of 1.38 being smaller than the true α value in this region.

The new temperature based on the measured α is believed to be the most accurate measurement on this flame to date. The factors affecting the temperature uncertainties considered here are mainly the uncertainties of α. The uncertainty of α_{ext} is expected to be small given the straightforward and well-established LOSA method and

good data quality (i.e., excellent goodness of fitting). The uncertainty of α_{sa}, however, is expected to be relatively large given that several assumptions and sources of uncertainty are included in deriving it. For example, Eq. (17) is based on the RDG approximation with uncertainty no better than 10 % [27, 47]; the uncertainties in the fundamental soot optical properties such as $E(m)$ and $F(m)$, and the uncertainty of k_0 all add uncertainties to α_{sa}, which makes formal uncertainty analysis particularly hard. However, the exponent α_{sa} generally ranges from 0.03 to 0.16 in the flame and is much smaller than α_{ext}. A sensitivity analysis on the effect of the dispersion exponent on the pyrometry-derived temperature has been performed. Varying dispersion exponent from 1 to 1.5 with an increment of 0.1 was used to calculate the soot spectral emissivity and therefore the temperature/color-ratio lookup tables. These lookup tables were then applied on the same measured color-ratio signal taken along the flame centerline to infer temperature. The derived temperature and the dispersion exponent being used are plotted in Fig. 20. As can be seen, a variation of 0.1 in the value of α results in ~ 10 K change in the pyrometry-derived temperature.

Since the value of α_{sa} is positive, the upper limit of α would be just α_{ext}. The temperature based on α_{ext}, in the case of neglecting the scattering component, could serve as a lower limit of the pyrometry-derived temperature given the fact that the temperature decreases with increasing α as seen in Fig. 20. The temperature based on α_{ext} without the scattering correction (the lower limit), the temperature based on α and their differences are shown in Fig. 21. The largest temperature difference of ~ 20 K occurs on the wings, and the temperature difference on the centerline is
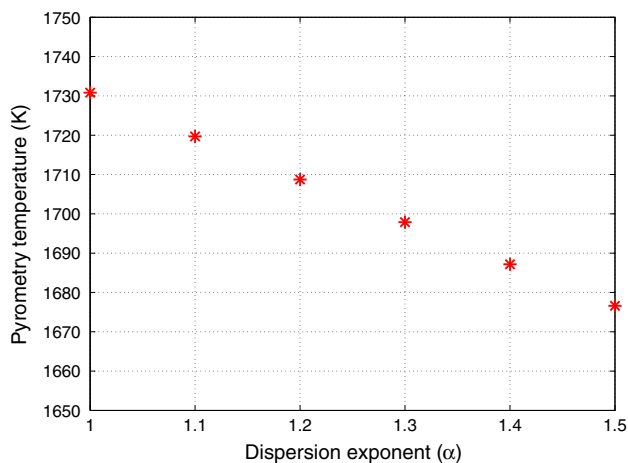
Fig. 20 The sensitivity of pyrometry measured temperature to the value of the dispersion exponent α
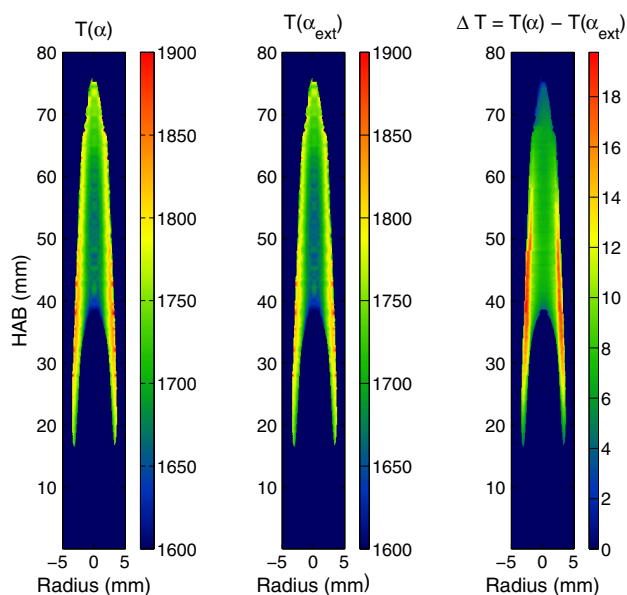

Fig. 21 The pyrometry temperatures based on α and α_{ext} and their differences

only ~8 K. If the current measured value of α_{sa} is larger than the actual value, the true temperature must be smaller than $T(\alpha)$ and greater than $T(\alpha_{ext})$ as shown in Fig. 21. If the measurement of α_{sa} on the flame centerline is smaller than the actual value by 0.1 (~100 %), the true temperature should be greater than the current $T(\alpha)$ by ~10 K according to the sensitivity analysis.

6 Conclusions

Combined optical characterizations of coflow laminar diffusions have been performed using multiple techniques. Traditional point multi-angle light scattering has been

extended to planar measurements. Spatially resolved soot radius of gyration was reported over the full flame region. Line-of-sight integrated extinction measurements were performed using spec-LOSA, from which two-dimensional spectral extinction coefficients were obtained after an Abel inversion. The spatially resolved dispersion exponent, α, was obtained in two dimensions by combining the results from multiple techniques. It was shown that the value of α varies with the degree of soot aging. A large value of α ~ 2 was obtained for young soot particles, and small value of ~0.9 was obtained for soot aggregates along the wings. The measured α was used to calculate soot spectral emissivities on a pixel-by-pixel basis, and the pyrometry temperature measurement was improved by using the spatially resolved α compared with using a "nominal" constant value. Finally, uncertainty analysis showed that the uncertainties in α_{sa} have a relatively small impact on pyrometry temperature on the order of ~20 K, and a lower temperature limit has been established in the case of neglecting the scattering component.

References

1. I. Glassman, Proc. Combust. Inst. **22**(1), 295–311 (1989)
2. C. Schulz, B.F. Kock, M. Hofmann, H. Michelsen, S. Will, B. Bougie, R. Suntz, G. Smallwood, Appl. Phys. B **83**(3), 333–354 (2006)
3. M. Hofmann, B.F. Kock, T. Dreier, H. Jander, C. Schulz, Appl. Phys. B **90**(3), 629–639 (2008)
4. K.A. Thomson, D.R. Snelling, G.J. Smallwood, F. Liu, Appl. Phys. B **83**(3), 469–475 (2006)
5. S. Will, S. Schraml, A. Leipertz, Opt. Lett. **20**(22), 2342–2344 (1995)
6. H.A. Michelsen, F. Liu, B.F. Kock, H. Bladh, A. Boiarciuc, M. Charwath, T. Dreier, R. Hadef, M. Hofmann, J. Reimann, S. Will, P.E. Bengtsson, H. Bockhorn, F. Foucher, K.P. Geigle, C. Mounaïm-Rousselle, C. Schulz, R. Stirn, B. Tribalet, R. Suntz, Appl. Phys. B **87**(3), 503–521 (2007)
7. J. Reimann, S.A. Kuhlmann, S. Will, Appl. Phys. B **96**(4), 583–592 (2009)
8. S. Will, S. Schraml, A. Leipertz, Proc. Combust. Inst. **26**(2), 2277–2284 (1996)
9. A. Jones, in *Light Scattering Reviews*, ed. by A. Kokhanovsky (Springer, Berlin, Heidelberg, 2006), pp. 393–444
10. C.M. Sorensen, Aerosol Sci. Technol. **35**(2), 648–687 (2001)
11. H. Oltmann, J. Reimann, S. Will, Appl. Phys. B **106**(1), 171–183 (2012)
12. H. Oltmann, J. Reimann, S. Will, Combust. Flame **157**(3), 516–522 (2010)
13. P.B. Kuhn, B. Ma, B.C. Connelly, M.D. Smooke, M.B. Long, Proc. Combust. Inst. **33**(1), 743–750 (2011)
14. B. Connelly. (2009). Quantitative characterization of steady and time-varying, sooting, laminar diffusion flames using optical

techniques (Doctoral dissertation). Yale University, http://guilford.eng.yale.edu/bcc_thesis.pdf

15. B. Ma, M.B. Long, Proc. Combust. Inst. **34**(2), 3531–3539 (2013)
16. B.C. Connelly, M.B. Long, M.D. Smoke, R.J. Hall, M.B. Colket, Proc. Combust. Inst. **32**, 777–784 (2009)
17. M.D. Smoke, M.B. Long, B.C. Connelly, M.B. Colket, R.J. Hall, Combust. Flame **143**(4), 613–628 (2005)
18. B.C. Connelly, B.A.V. Bennett, M.D. Smoke, M.B. Long, Proc. Combust. Inst. **32**(1), 879–886 (2009)
19. http://www.adelaide.edu.au/cet/isfworkshop/data-sets/laminar/ (12/2013)
20. S. Gangopadhyay, I. Elminyawi, C.M. Sorensen, Appl. Opt. **30**(33), 4859–4864 (1991)
21. K.A. Thomson, M.R. Johnson, D.R. Snelling, G.J. Smallwood, Appl. Opt. **47**(5), 694–703 (2008)
22. D.R. Snelling, K.A. Thomson, G.J. Smallwood, Ö.L. Gülder, Appl. Opt. **38**(12), 2478–2485 (1999)
23. H. Zhao, N. Ladommatos, Prog. Energy Combust. Sci. **24**(3), 221–255 (1998)
24. B.S. Haynes, H. Jander, H.G. Wagner, Ber. Bunsenges. Phys. Chem. **84**(6), 585–592 (1980)
25. P.S. Greenberg, J.C. Ku, Appl. Opt. **36**(22), 5514–5522 (1997)
26. A.R. Coderre, K.A. Thomson, D.R. Snelling, M.R. Johnson, Appl. Phys. B **104**(1), 175–188 (2011)
27. F. Migliorini, K. Thomson, G. Smallwood, Appl. Phys. B **104**(2), 273–283 (2011)
28. C.M. Sorensen, J. Cai, N. Lu, Appl. Opt. **31**(30), 6547–6557 (1992)
29. MATLAB version 8.1.0. Natick, Massachusetts: The MathWorks Inc., 2013
30. C.A. Glasbey, K.V. Mardia, J. Appl. Stat. **25**(2), 155–171 (1998)
31. F. Liu, K.A. Thomson, G.J. Smallwood, Combust. Flame **160**(9), 1693–1705 (2013)
32. C.J. Dasch, Appl. Opt. **31**(8), 1146–1152 (1992)
33. K.M. Martin. *Acoustic modification of sooting combustion* (Doctoral dissertation). The University of Texas at Austin, 2002
34. S. De Iuliis, F. Cignoli, S. Benecchi, G. Zizak, Appl. Opt. **37**(33), 7865–7874 (1998)
35. R.C. Millikan, J. Opt. Soc. Am. **51**(6), 698–699 (1961)
36. H.C. Hottel, F.P. Broughton, Ind. Eng. Chem. Anal. Ed. **4**(2), 166–175 (1932)
37. S. De Iuliis, M. Barbini, S. Benecchi, F. Cignoli, G. Zizak, Combust. Flame **115**(1–2), 253–261 (1998)
38. A. D'Alessio, F. Beretta, C. Venitozzi, Combust. Sci. Technol. **5**(1), 263–272 (1972)
39. C.R. Shaddix, Á.B. Palotás, C.M. Megaridis, M.Y. Choi, N.Y.C. Yang, Int. J. Heat Mass Transf. **48**(17), 3604–3614 (2005)
40. C.M. Sorensen, G.C. Roberts, J. Colloid Interface Sci. **186**(2), 447–452 (1997)
41. R.D. Mountain, G.W. Mulholland, Langmuir **4**(6), 1321–1326 (1988)
42. Ü.Ö. Köylü, G.M. Faeth, T.L. Farias, M.G. Carvalho, Combust. Flame **100**(4), 621–633 (1995)
43. S.S. Krishnan, K.C. Lin, G.M. Faeth, J. Heat Transf. **122**(3), 517–524 (2000)
44. B.J. Stagg, T.T. Charalampopoulos, Combust. Flame **94**(4), 381–396 (1993)
45. H. Chang, T.T. Charalampopoulos, Proc. Math. Phys. Sci. **430**(1880), 577–591 (1990)
46. B. Ma, G. Wang, G. Magnotti, R.S. Barlow, M.B. Long, Combust. Flame **161**(4), 908–916 (2014)
47. T.L. Farias, U.O. Köylü, M.G. Carvalho, Appl. Opt. **35**(33), 6560–6567 (1996)